Biomechanical coupling facilitates spinal neural tube closure in mouse embryos

Gabriel L. Galea[a,1], Young-June Cho[a], Gauden Galea[b], Matteo A. Molè[a,2], Ana Rolo[a,3], Dawn Savery[a], Dale Moulding[a], Lucy H. Culshaw[a], Evanthia Nikolopoulou[a], Nicholas D. E. Greene[a], and Andrew J. Copp[a]

[a]Newlife Birth Defects Research Centre, UCL Great Ormond Street Institute of Child Health, University College London, London WC1N 1EH, United Kingdom; and [b]Division of Noncommunicable Diseases and Promoting Health Through the Life Course, World Health Organization Regional Office for Europe, Copenhagen DK-2100, Denmark

Edited by Ray Keller, University of Virginia, Charlottesville, VA, and accepted by Editorial Board Member Kathryn V. Anderson May 16, 2017 (received for review January 20, 2017)

Neural tube (NT) formation in the spinal region of the mammalian embryo involves a wave of "zippering" that passes down the elongating spinal axis, uniting the neural fold tips in the dorsal midline. Failure of this closure process leads to open spina bifida, a common cause of severe neurologic disability in humans. Here, we combined a tissue-level strain-mapping workflow with laser ablation of live-imaged mouse embryos to investigate the biomechanics of mammalian spinal closure. Ablation of the zippering point at the embryonic dorsal midline causes far-reaching, rapid separation of the elevating neural folds. Strain analysis revealed tissue expansion around the zippering point after ablation, but predominant tissue constriction in the caudal and ventral neural plate zone. This zone is biomechanically coupled to the zippering point by a supracellular F-actin network, which includes an actin cable running along the neural fold tips. Pharmacologic inhibition of F-actin or laser ablation of the cable causes neural fold separation. At the most advanced somite stages, when completion of spinal closure is imminent, the cable forms a continuous ring around the neuropore, and simultaneously, a new caudal-to-rostral zippering point arises. Laser ablation of this new closure initiation point causes neural fold separation, demonstrating its biomechanical activity. Failure of spinal closure in pre-spina bifida *Zic2*^{Ku} mutant embryos is associated with altered tissue biomechanics, as indicated by greater neuropore widening after ablation. Thus, this study identifies biomechanical coupling of the entire region of active spinal neurulation in the mouse embryo as a prerequisite for successful NT closure.

neural tube | biomechanics | F-actin | Zic2 | mouse

Neural tube (NT) defects (NTDs) are severe neurodevelopmental disorders that affect ∼1 in every 1,000 births (1). NTDs arise from failure of NT closure in early gestation. In mammals, NT closure is initiated at multiple sites known as "closure points," with closure 1 at the hindbrain/cervical boundary initiating cephalic and spinal neurulation. Spinal NT formation involves a wave of "zippering" that moves in a rostral-to-caudal direction along the elongating spinal axis (2–4). The region of closing NT caudal to the "zipper" is called the posterior neuropore (PNP). The PNP is composed of lateral neural folds flanking a midline neural plate that caudally contains bipotential neuromesodermal progenitors (NMPs) (5). During spinal neurulation, the neural folds elevate progressively and are apposed medially, uniting at the zippering point to create the roof of the newly formed NT covered by surface ectoderm. Failure of this closure process leads to open spina bifida (myelomeningocoele). Failure of zippering at different somite levels results in spina bifida lesions of corresponding lengths. For example, zinc finger protein of the cerebellum (*Zic*) *2* loss-of-function (*Kumba* mutant) homozygous mutant mice, in which zippering fails around the 15-somite stage, develop a large spina bifida extending from the thoracic level caudally (6).

A persistent challenge in determining and ultimately preventing the developmental bases of spina bifida is the absence of a unified biomechanical understanding of the tissue deformations required for progression of NT closure. Biomechanical descriptions of vertebrate NT closure date back to the 19th century (7) and evolved in the 20th century to encompass mechanical etiologies of NTDs described as "mechanical teratogenesis" (8). The view that abnormal tissue mechanics may underlie failure of NT closure has been substantiated by experimental interventions in mouse and chicken embryos in which altered ventral curvature was seen to delay or prevent completion of spinal NT closure (9, 10).

The demonstration that extrinsic forces can prevent NT closure implies that sufficient forces are normally generated to achieve closure. The nature of the cellular "motor(s)" required for the initiation, progression and completion of NT closure remains incompletely understood, however. Studies in experimentally tractable ascidians and lower vertebrates have mapped mechanical stresses that are normally withstood within and around the neuroepithelium. This work has identified cellular behaviors, such as actomyosin-driven apical constriction of neural plate cells, required to initiate apposition of the neural folds (11–16). Genetic or pharmacologic disruption of actin remodeling enzymes prevents NT closure in amphibians as well as in mice (16–19). Moreover, progression of neurulation in mice

Significance

Neurulation has been intensively studied in lower vertebrates, but marked species differences call into question the relevance of these models for human neural tube (NT) closure. Here, using mouse embryos, we demonstrate that mammalian neural fold apposition results from constriction of the open posterior NT, which is biomechanically coupled to the zippering point by an F-actin network. Using the *Zic2* mutant model, we show that genetic predisposition to spina bifida, which likely underlies most human cases, directly affects the biomechanics of closure. We also identify a NT closure point at the caudal end of the embryo. Many spina bifida cases correspond to this anatomic portion of the NT, suggesting that this closure point may be important in humans as well.

Author contributions: G.L.G., Y.-J.C., G.G., N.D.E.G., and A.J.C. designed research; G.L.G., Y.-J.C., G.G., M.A.M., A.R., D.S., D.M., L.H.C., and E.N. performed research; G.L.G., N.D.E.G., and A.J.C. contributed new reagents/analytic tools; G.L.G., Y.-J.C., M.A.M., A.R., N.D.E.G., and A.J.C. analyzed data; and G.L.G., N.D.E.G., and A.J.C. wrote the paper.

The authors declare no conflict of interest.

This article is a PNAS Direct Submission. R.K. is a guest editor invited by the Editorial Board.

[1]To whom correspondence should be addressed. Email: g.galea@ucl.ac.uk.

[2]Present address: Mammalian Embryo and Stem Cell Group, Department of Physiology, Development, and Neuroscience, University of Cambridge, Cambridge CB2 3DY, United Kingdom.

[3]Present address: Centre for Craniofacial and Regenerative Biology, King's College London, London SE1 9RT, United Kingdom.

This article contains supporting information online at www.pnas.org/lookup/suppl/doi:10.1073/pnas.1700934114/-/DCSupplemental.

requires cytoskeleton-rich cellular protrusions from nonneural ectoderm cells directly ahead of the zippering point (4, 20).

In silico simulations of amphibian embryos predict that mechanical tension within the surface ectoderm and other tissues surrounding the NT serves to oppose neural fold apposition (13). Indeed, tension within the nonneural ectoderm of amphibian embryos has been repeatedly demonstrated by documenting immediate retraction (i.e., widening) of microsurgical incisions or laser ablations (12, 21–23); however, these methods do not identify the source of tension and are difficult to apply to large regions of tissue, such as the PNP, which exceeds 0.6 mm in length at early somite stages. Application of tensile stress to elastically deformable structures (24) results in extension, leading to the structure experiencing strain (defined as the percentage change in dimension). Strain can be measured noninvasively through such engineering techniques as digital image correlation (DIC). DIC maps the relative location of preplaced dots on the surface of structures such as bone imaged before vs. after deformation to calculate strains experienced (25, 26). Disadvantages of current DIC methodologies applied to biological tissues include the requirement for a high-resolution dot pattern, "noisy" data owing to errors in automated dot mapping, and the limitation of producing 2D/pseudo-3D analyses. Adaptations of DIC-like methodologies to biological tissues include the use of fluorescent-labeled cells instead of preplaced dots as the mapped entity (27).

In the present study, we applied DIC, as well as a purpose-built tissue deformation and strain measurement (TDSM) workflow, to infer tissue stresses within and around the zippering spinal NT from the displacement of mosaic fluorescent-labeled cells after mechanical disruption of the zippering point. Using these methods, together with live mouse embryo imaging, we set out to determine the role and location of the biomechanical influences that influence neural fold apposition during mouse spinal NT closure.

Results

Neural Fold Midline Apposition Is Opposed by Tension Within the Surrounding Tissues. We initially observed that progressive narrowing of the PNP is opposed by mechanical tensions within the associated tissues. During spinal neurulation, the PNP shortens and narrows with advancing somite stage, owing to progressive zippering and midline apposition of the elevated neural folds (28) (Fig. 1 *A* and *B*). In silico simulations of neurulation in lower vertebrates have predicted that neural fold midline apposition is opposed by stresses within laterally tethering tissues (13). Consistent with this idea, we observed that in intact living mouse embryos, needle incision of the zippering point and most recently closed NT roof resulted in immediate widening of the PNP due to lateral displacement of the neural folds (Fig. 1 *C* and *D* and Movie S1). The same effect was seen when the zippering point is laser-ablated in live-imaged embryos (Fig. 1 *E* and *F*). Neural fold displacement and widening of the PNP not only affected the ablated region, but also extended more than 75% of the length of the open PNP (i.e., ∼200 μm caudal to the zippering point; Fig. 1*G*).

To infer the mechanical stresses "withstood" by the zippering point, we applied two methods to map tissue displacement and relative change in dimension ("strain", ε) within and around the PNP before vs. after laser ablation of the zippering point. We first implemented DIC using two previously reported systems: Moiré DIC (29), available at opticist.org/, and improved DIC (30), available through MathWorks.com. We then developed and applied a TDSM workflow able to quantify 3D changes in tissue dimensions (*SI Appendix*, section 1, Fig. S1, with further documentation in *SI Appendix*, section 2). The basis of TDSM is the analysis of deformation of a 3D Delaunay triangulation matrix between cell centroids (Fig. 2*A* and *SI Appendix*, section 1, Fig. S1). Moiré DIC, improved DIC, and TDSM all accurately quantified simulated uniaxial strains, but the latter two techniques outperformed Moiré DIC at low strain magnitudes (*SI Appendix*, section 2). Improved DIC provides data on von Mises strain, a

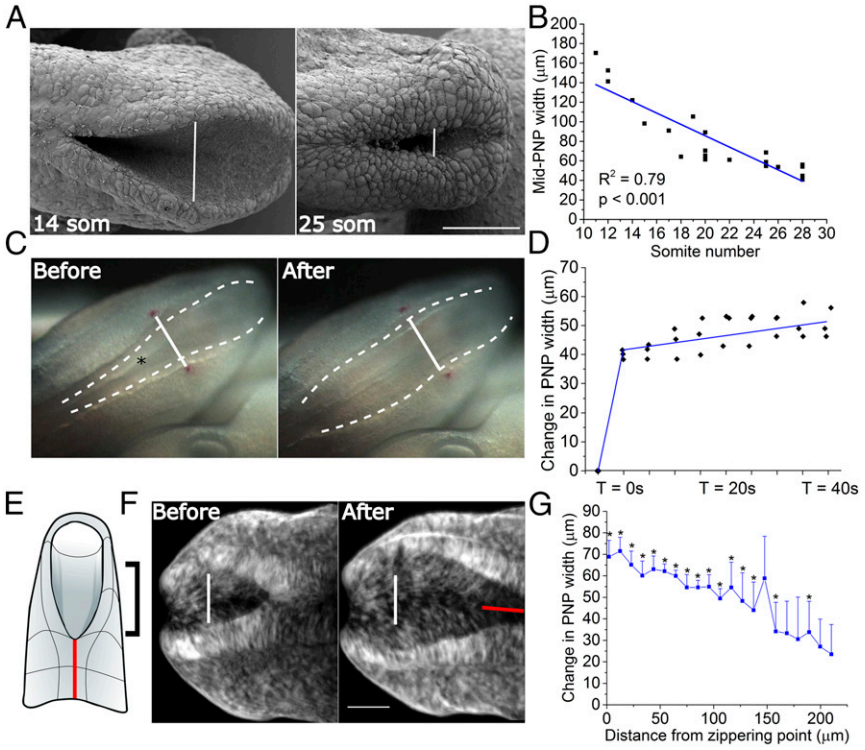

Fig. 1. Midline apposition of the neural folds is opposed by mechanical tension. (*A*) Representative scanning electron micrographs of mouse PNPs at two stages of development (somite stages indicated), showing the reduction in PNP width (solid lines) with advancing stage. Rostral is to the left side; caudal, to the right side. (Scale bar: 100 μm.) (*B*) Quantification of the width of the PNP at its midpoint at the indicated somite stages, demonstrating that the PNP gradually narrows as it closes. (*C*) Representative images showing widening of the PNP (dashed lines) after needle incision of the zippering point (asterisk). The solid white line indicates the distance between DiI labels before incision (Movie S1). (*D*) Quantification of the change in PNP width (final width – initial width) at the indicated times after needle incision of the zippering point, demonstrating the rapid increase in PNP width. (*E*) Schematic illustration of the region ablated with needle or laser (red line) and the approximate region in which widening of the open PNP was quantified (black bracket). (*F*) Representative images of a live-imaged embryo PNP before and after laser ablation. The white line indicates PNP width before ablation; the red line indicates the ablated NT region. (*G*) Quantification of the change in PNP width after completion of laser ablation (Z-stack capture completed ∼4 min after ablation). The change in width was measured every 10 μm caudally from the zippering point. PNP width increased after ablation at least 200 μm caudal to the ablation site. Points represent mean ± SEM, $n = 5$ embryos. *$P < 0.05$ (width before vs. after), repeated-measures ANOVA with Bonferroni post hoc correction.

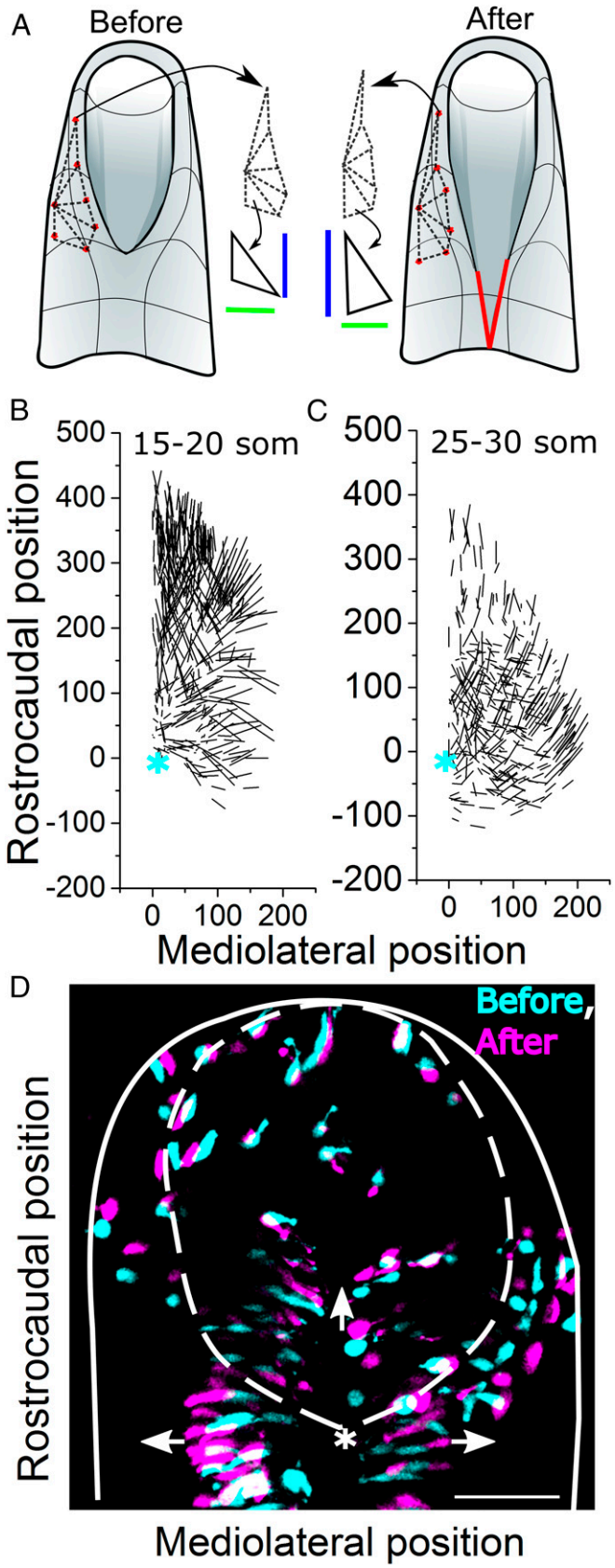

Fig. 2. The PNP zippering point is under lateral and caudally oriented stresses. (*A*) Schematic representation of the TDSM methodology (expanded in *SI Appendix*, section 1, Fig. S1 and *SI Appendix*, section 2). Centroids of mosaic fluorescent cells (red dots) are linked 3-dimensionally in a Delaunay triangulation mesh. Changes in triangle dimensions are used to calculate strain. Displacement of the triangulation centroids provides displacement vectors. (*B* and *C*) TDSM displacement analysis of 15- to 20-somite (*B*) and 25- to 30-somite (*C*) stage embryos illustrating 2D displacement vectors of triangulation centroids. Vector lengths indicate the magnitude of displacement, and orientation indicates the direction of displacement after zippering point laser ablation (the zippering point at the origin, indicated by asterisks, is taken as the reference point). Data are shown as the aggregate of points from three embryos at each stage. (*D*) Representative registered image of a 25-somite embryo in which fluorescent cells are produced via mosaic recombination of the mTmG transgene, driven by β-actin CreERT2. This illustrates the caudal and lateral displacement (arrows) of cells following zippering point (*) ablation relative to the zippering point (before ablation, cyan; after ablation, magenta). The outline of the PNP is indicated by the white dashed line. (Scale bar: 100 μm.)

measure used to predict mechanical failure based on distortion energy, which can be calculated independent of rotation. Previous biological studies have reported area strain (percentage change in area) as a similarly rotation-independent measure (31, 32). Therefore, we used the percentage change in 2D surface area of each triangulation in the 3D mesh to calculate area strain in TDSM (*SI Appendix*, section 2).

Application of TDSM to confocal stacks of live-imaged mouse embryos revealed that in addition to mediolateral displacement expected from the observed PNP widening, zippering point ablation also caused displacement of cells caudal to the zippering point (used as the reference point) in a caudoventral direction (Fig. 2 *B* and *C*). The caudoventral region of the PNP corresponds to the location identified as containing NMPs (5), and thus is referred to as the "NMP zone" hereinafter. Caudal displacement predominates in the open PNP, whereas lateral displacement is predominantly seen lateral to the zippering point and over the neural folds. Caudal and lateral displacement of neuroepithelial and mesodermal cells is also apparent in registered images (Fig. 2*D*). Applying improved DIC (Fig. 3 *A* and *B*) or TDSM (Fig. 3 *C* and *D*) analysis, we observed that zippering point ablation resulted predominantly in expansion of the adjacent tissue and neural folds in embryos with 15–20 or 25–30 somites. This finding was unexpected, because if the zippering point had been pulling adjacent tissue toward the midline, that tissue would have been expected to relax to a smaller size (negative area strain) after zippering point ablation. As a control, embryos were fixed in paraformaldehyde before laser ablation (since fixation dissipates tissue stresses); these embryos did not show significant deformations (*SI Appendix*, section 1, Fig. S2).

Taken together, these findings suggest that progressive midline apposition of the neural folds overcomes opposing mechanical tensions. Consequently, when the structural integrity of the zippering point is compromised, the neural folds recoil into a more lateral position, with tissue expansion and widening of the PNP.

Constriction of the NMP Zone Draws the Neural Folds Medially. Strain mapping of live imaged embryos suggested that the NMP zone exists in a dynamic force equilibrium with the zippering point—that is, its constriction is normally limited by the tethering effect of the intact PNP, but it constricts further when the zippering point is mechanically disrupted. In contrast to expansion of tissue around the ablated zippering point, a distinct region of constriction/compression was observed corresponding to the NMP zone (Fig. 3 *A*–*D*). Compression of the caudoventral PNP after zippering point ablation was confirmed using a more targeted Cre driver (Nkx1-2; Fig. 3*E*) and selective TDSM analysis of this zone (Fig. 3*F*), which avoided the confounding effects of surrounding tissues extending toward it. Regional area strain analyses

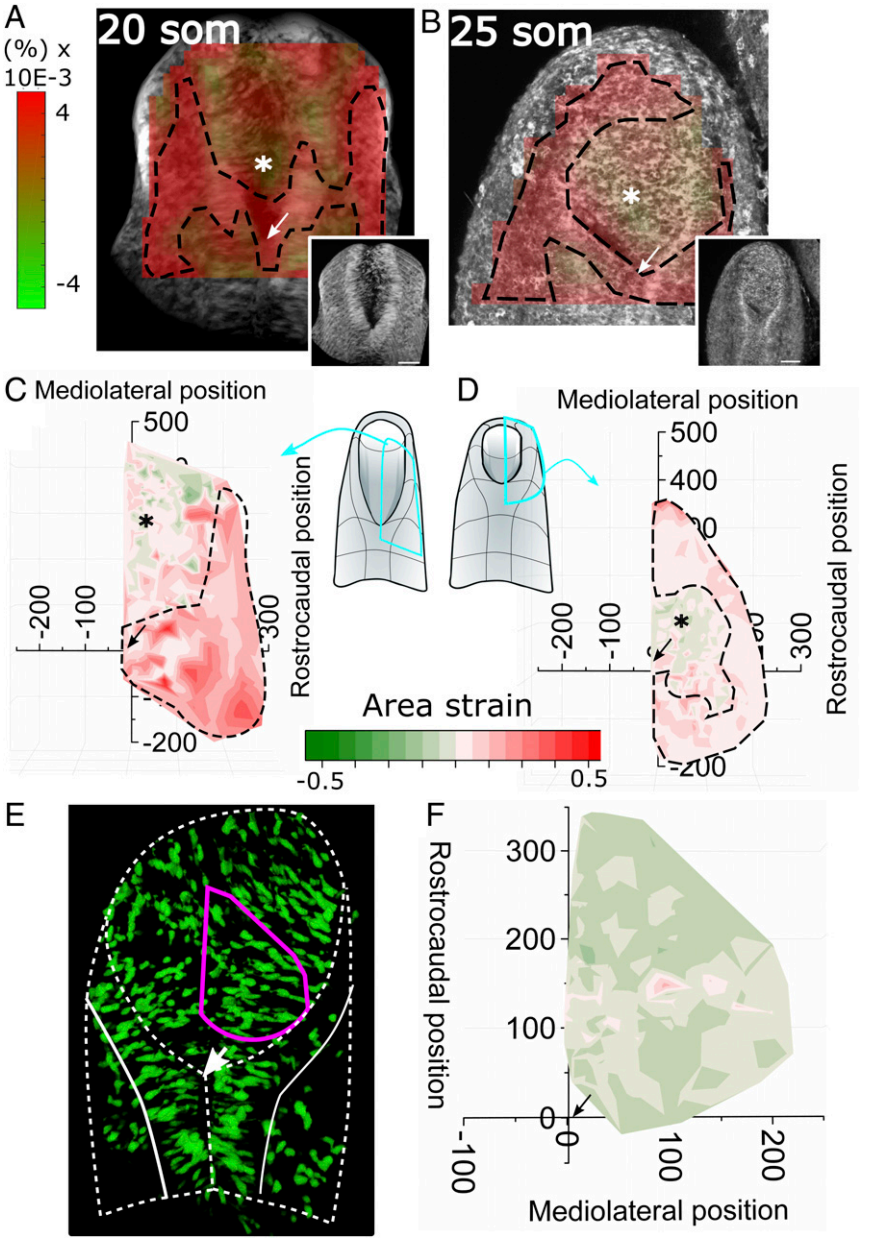

Fig. 3. PNP zippering point ablation results in predominant tissue expansion around the zippering point and constriction of the NMP zone. (*A–D*) Improved DIC von Mises strain maps (*A* and *B*) and TDSM area strain maps (*C* and *D*) of representative 15- to 20-somite (*A* and *C*) and 25- to 30-somite (*C* and *D*) embryos. The maps reveal tissue expansion (red, outlined with dashed lines) around the zippering point (arrows) and neural folds after ablation, whereas tissue compression (*) is predominantly observed caudal to the zippering point, in the midline NMP zone. (*E*) Representative live-imaged PNP of a 20-somite Nkx1-$2^{CreERT2}$; $ROSA^{YFP}$ mouse embryo illustrating the NMP zone region analyzed by TDSM (magenta line) caudal and ventral to the zippering point (arrow). (*F*) Area strain map selectively analyzing Nkx1-$2^{CreERT2}$-expressing cells in the region shown in *E*, confirming predominant tissue constriction (green) in this region following laser ablation of the zippering point (arrow), despite the previously demonstrated overall widening of the PNP. TDSM maps are in the orientations shown in the insets in *A* and *B*. Although the TDSM analyses are presented in 2D for publication purposes, they were all performed in 3D, taking into account each cell's *x*, *y*, and *z* centroid positions.

confirmed significant expansion of tissue rostral to and significant compression of tissue caudal to the zippering point (*SI Appendix*, section 1, Fig. S2*B*). Thus, ablation of the zippering point causes far-reaching deformation, suggesting that the zippering point is biomechanically coupled to the NMP zone.

To visualize these dynamic behaviors, we developed a system of medium-term live embryo imaging that allows analysis of changes in cellular apical surface area, as well as observation of continued apposition of the neural folds (Fig. 4*A*). The apical surface area of NMP zone cells decreased relative to their initial size during 1 h of live imaging (Fig. 4*B*), documenting in mammalian embryos a process that is known to biomechanically mediate neural fold midline approximation in lower vertebrates (14, 19, 33). The surface area of surface ectoderm cells immediately rostral to the zippering point did not change significantly over the same time period (*SI Appendix*, section 1, Fig. S3 *A* and *B*). Overall PNP length tended to decrease over the period, with occasional observation of zippering point cellular protrusions consistent with ongoing closure (*SI Appendix*, section 1, Fig. S3 *C* and *D*). Medial apposition of the neural folds resulted in significant

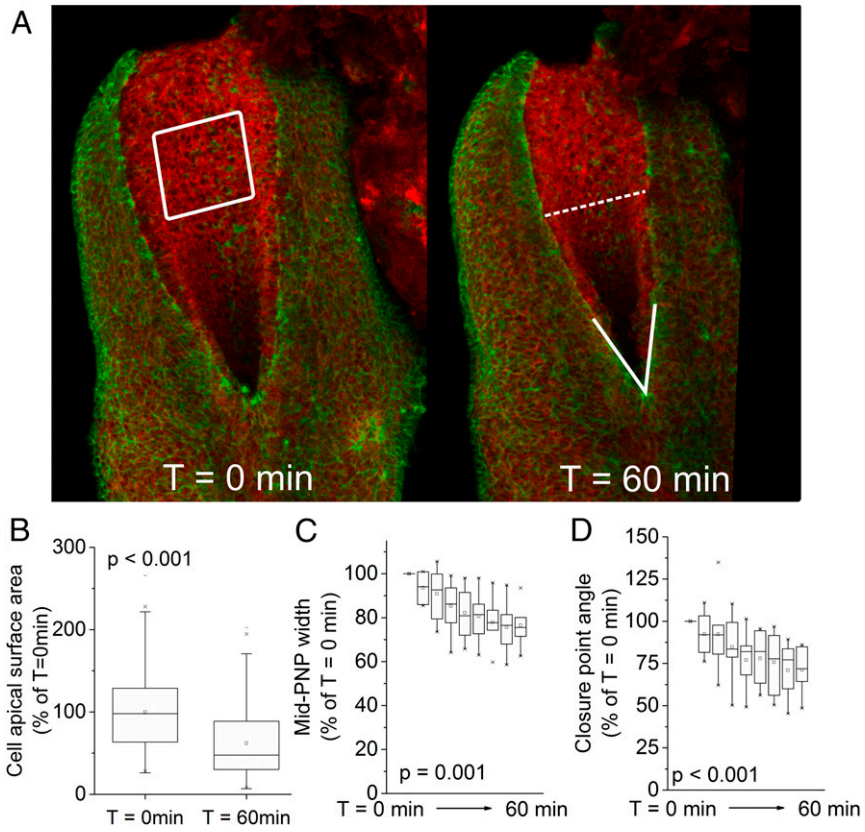

Fig. 4. Neural fold midline apposition is associated with constriction of the NMP zone. (*A*) Representative frames of a live-imaged Grhl3Cre; mTmG mouse embryo (~18 somites) at $T = 0$ min and $T = 60$ min (Movie S2). The white box indicates the NMP zone, analyzed in *B*; the dashed line indicates mid-PNP width; and the white "V" indicates the zippering point angle. (*B*) Quantification of the apical surface areas in the NMP zone of live-imaged mTmG embryos based on tdTomato-labeled membrane at $T = 0$ min and $T = 60$ min demonstrating a reduction in size consistent with apical constriction, a mechanism whereby the NMP zone may undergo constriction. Data represent 30 cell surface areas from each of seven embryos. *P* values indicate the differences between the two groups by the Wilcoxon signed-rank test. (*C* and *D*) Quantification of the mid-PNP width (*C*) and zippering point angle (*D*) over 60 min of live imaging relative to the initial measurement for each embryo ($T = 0$ min set at 100%); $n = 7$. These analyses demonstrate the continued (or resumed) apposition of the neural folds and constriction of the NMP zone cells under live embryo imaging conditions. *P* values in *C* and *D* indicate significant change over time by mixed model analysis, accounting for repeated measures from each embryo.

reductions in PNP width and zippering point angle (Fig. 4 *C* and *D*). Dorsoventral cell displacement, as a potential basis for PNP narrowing, was minimal over the same period (*SI Appendix*, section 1, Fig. S4).

Taken together, the results of strain mapping and live imaging analysis suggest that the continuation of PNP closure is associated with selective constriction of NMP zone cells, aiding the apposition of the neural folds in the midline and thereby narrowing the zippering point angle across which cellular protrusions must reach.

A Wide-Ranging F-Actin Network Biomechanically Couples the PNP. We found that biomechanical coupling of the zippering point to the NMP zone involves a supracellular F-actin network extending between these structures. In mouse embryos, apical actomyosin enrichment has been documented in the NMP zone (17) (*SI Appendix*, section 1, Fig. S5*A*), as well as in the neuroepithelium of the closing NT (34). Whole-mount imaging of phalloidin-stained mouse embryos confirmed the presence of a dense F-actin network in the NMP zone and revealed the presence of a long F-actin cable emanating from the zippering point and running caudally along the neural folds (Fig. 5*A* and *SI Appendix*, section 1, Fig. S5*B*). This cable was seen to colocalize with the surface ectoderm adherens junction marker E-cadherin at the surface ectoderm–neuroepithelial boundary (Fig. 5*B*), forming a continuous structure across cell junctions (*SI Appendix*, section 1, Fig. S5*B*).

In embryos at early somite stages with long PNPs, the cable could be >0.5 mm long and still not fully encircle the PNP (Fig. 5*A*). At later stages, when the PNP had shortened to <~300 μm (*SI Appendix*, section 1, Fig. S6 *A–D*), the cable encircled the PNP, forming an elongated "purse string"-like structure (Fig. 5*C*). This association between cable length and PNP length held true in embryos from wild-type mice maintained on three different background strains (*SI Appendix*, section 1, Fig. S6). The transition to the F-actin cable encircling the PNP is marked by a dramatic change in PNP shape distally, from an early "spade"-like structure to a late-stage elliptical structure. F-actin staining revealed enrichment at both the zippering point and at the caudal-most PNP canthus in late-stage PNPs (Fig. 5*C*). Moreover, scanning electron microscopy detected cellular protrusions (20) at both sites (Fig. 5*D*). This suggests that, when completion of closure is imminent, a new zippering point forms at the caudal extremity of the PNP.

A New Caudal Closure Point Forms When Completion of Spinal Neurulation Is Imminent. The caudal canthus of the late-stage PNP biomechanically facilitates neural fold apposition. We refer to this caudal closure point as closure 5 (cyan arrow in Fig. 5*C*). Closure 5 has been hypothesized to exist in mice based on the morphology of late-stage PNPs (35), as well as in humans based on the distribution of spina bifida lesions (36, 37), but its existence

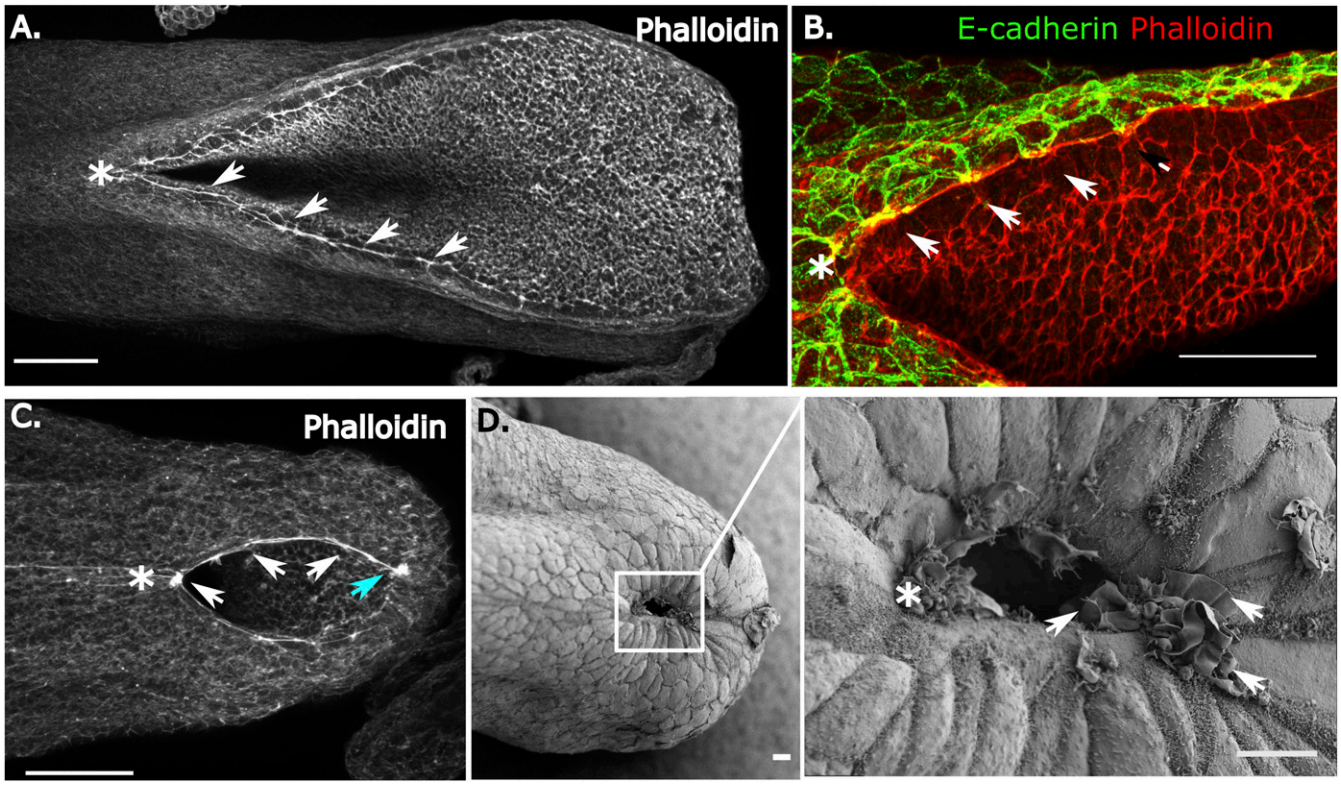

Fig. 5. A long-ranging F-actin network biomechanically couples the mammalian closing spinal NT. (*A*) PNP region of a representative 14-somite embryo stained with phalloidin to illustrate the presence of an F-actin cable (arrows) that runs caudally from the zippering point (*) along the closing neural folds. (Scale bar: 100 μm.) (*B*) This cable at the surface ectoderm-neuroepithelial boundary colocalises with the surface ectoderm adherens junction marker E-cadherin (arrows). (Scale bar: 20 μm.) (*C*) At later somite stages, when completion of PNP closure is imminent, this cable encircles the PNP (30-somite stage shown, cyan arrow indicates the caudal PNP canthus). (Scale bar: 100 μm.) (*D*) At this stage, cellular protrusions are visible at the caudal extremity (canthus) of the PNP (arrows in the higher-magnification scanning electron microscope image on the right) as well as at the zippering point (*). These features indicate formation of a new zippering point (closure 5), as well as the continued presence of the original zippering point (*) at the rostral extremity of the PNP. (Scale bars: 10 μm.)

has never been conclusively demonstrated. To determine whether closure 5 contributes to neural fold apposition, we laser-ablated it in live-imaged 25- to 30-somite mouse embryos. Ablation of the F-actin ring at closure 5 resulted in widening of the PNP, as did ablation of the ring at the rostral PNP zippering point (Fig. 6 *A*, *C*–*E*). In contrast, ablation of the caudal tip of the PNP in 15- to 20-somite embryos, before the formation of closure 5, did not result in significant PNP widening, whereas ablation of the F-actin cable at the zippering point or along the neural folds caused widening of the PNP (Fig. 6*D*). We hypothesized that the observed PNP widening after ablation at the zippering point, at closure 5, or along the neural folds is related to disruption of the F-actin network.

To test this idea further, we acutely inhibited actin by a 15-min treatment with Latrunculin B (LatB), which resulted in dose-dependent PNP widening (*SI Appendix*, section 1, Fig. S7). Thus, the F-actin network biomechanically couples the PNP and facilitates drawing of the neural folds toward the midline, such that ablating the F-actin cable at the zippering point, along the neural folds, or at closure 5, or pharmacologically severing F-actin with LatB causes the neural folds to move apart, resulting in widening of the PNP.

The Biomechanics of Neural Fold Apposition Are Altered by Mutations in *Zic2*. Biomechanical alterations may underlie faulty NT closure in a mouse model of severe spina bifida. This was inferred from the change in PNP width observed after zippering point ablation in *Kumba* ($Zic2^{Ku}$) mutants, which carry a functionally null allele of the transcription factor Zic2 (38). $Zic2^{Ku/Ku}$ embryos show dramatically enlarged PNPs with 100% penetrance at late neurulation stages, but at the 12- to 15-somite stage, total PNP length is not yet significantly altered (representative examples in Fig. 7*A*). At this stage, the F-actin cable is clearly visible along the neural folds in $Zic2^{+/+}$ and $Zic2^{Ku/+}$ embryos, but only short segments are visible in $Zic2^{Ku/Ku}$ embryos (Fig. 7*A*). PNP widening is observed in all three genotypes after laser ablation of the zippering point, but widening was significantly greater in $Zic2^{Ku/Ku}$ embryos than in wild-type littermates, particularly just caudal to the zippering point (Fig. 7*B*). Greater PNP widening in $Zic2^{Ku/Ku}$ embryos compared with $Zic2^{+/+}$ embryos was also observed after microsurgical incision of the zippering point (*SI Appendix*, section 1, Fig. S8). $Zic2^{Ku/+}$ embryos, which do successfully close their PNP, exhibited significantly greater widening than $Zic2^{+/+}$ littermates at various points along the open PNP. These observations suggest that genetically-influenced alterations in the biomechanics of spinal closure may underlie spina bifida in this mammalian model.

Discussion

Mammalian spinal neurulation is a biomechanical event requiring midline apposition of the neural folds, which narrows the PNP as it shortens through zippering. Inference of cellular biomechanics by laser ablation in simpler organisms is well-established (11, 39–42), but is substantially complicated in mouse embryos by their comparatively large size, complex shape, and tissue opacity. Here we investigated the effects of needle and laser ablations on tissue morphology many cell diameters away from the ablation site in

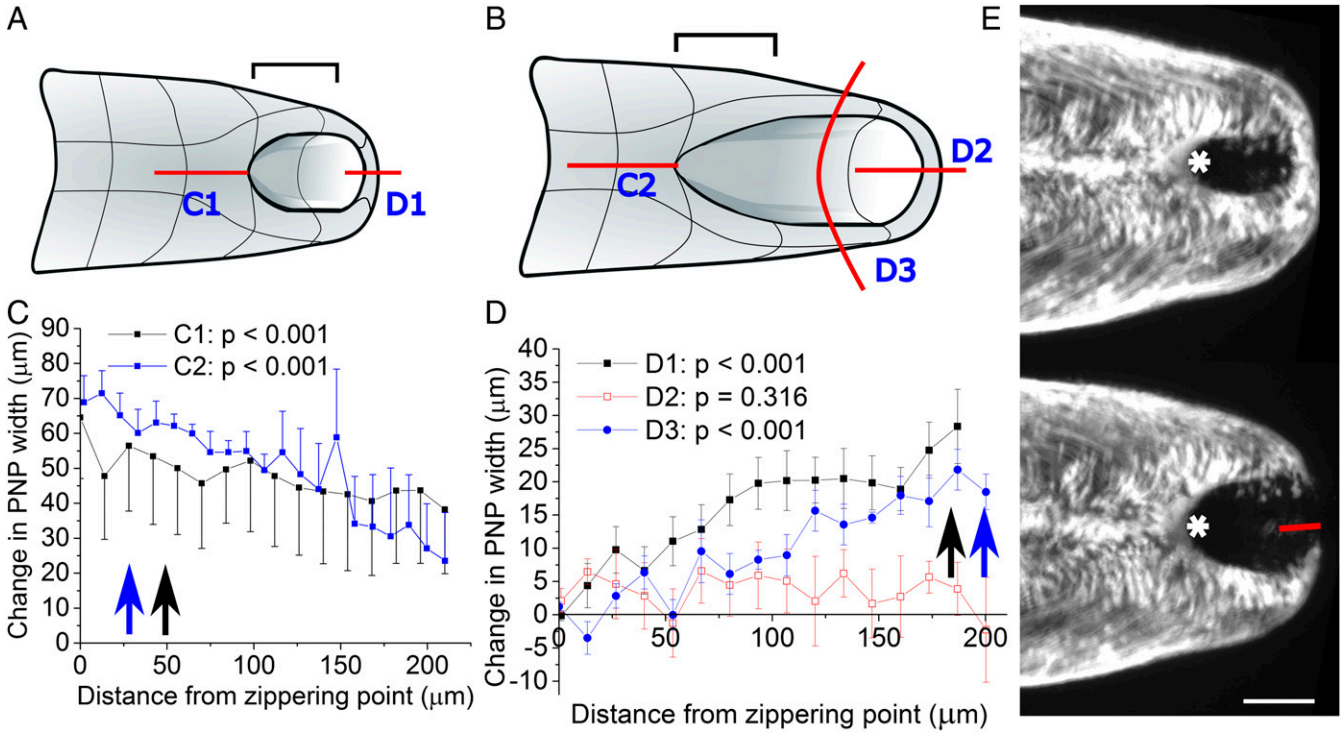

Fig. 6. Laser ablation of the F-actin cable causes PNP widening. The F-actin cable was disrupted with a series of laser ablations. (*A*) Two types of ablation were made in embryos at late somite stages (25–30 somites), when a complete F-actin ring has formed. The rostral extremity (zippering point, C1) or caudal extremity (closure 5, D1) of the PNP were ablated (red lines). (*B*) Three types of ablations were made at earlier somite stages (15-20 somites). The zippering point was ablated (C2) as shown in Fig. 1, caudoventral midline ablations paralleled the closure 5 ablations performed at later somite stages (D2), and the F-actin cable was ablated along the neural folds (D3). The ablations in the schematics are labeled to correspond with the analysis of changes in PNP width in the region, indicated by the black brackets above each schematic. (*C* and *D*) Change in PNP width at different positions along the PNP following ablations. The zippering point is at $x = 0$ in each graph. Zippering point ablation at both somite stages (C1/C2; $n = 5$ in each case) results in PNP widening, most markedly near the zippering point (arrows) but also extending more than 200 μm caudally along the PNP. Ablations of closure 5 (D1; $n = 8$) or through the neural folds (D3; $n = 6$) increase PNP width caudal to the zippering point (arrows), whereas the zippering point itself is not disrupted. Caudoventral ablations before the formation of closure 5 (D2; $n = 4$) do not significantly change PNP width (red line in *D*). *P* values indicate the overall differences comparing neural fold distance before and after ablation, accounting for repeated measures from the same embryo at different rostrocaudal positions by mixed model analysis. (*E*) Representative frames of a live-imaged 29-somite embryo PNP before and after closure 5 ablation. Note the widening of the entire PNP after ablation. *Zippering point. The red line indicates ablation. (Scale bar: 100 μm.)

live-imaged embryos. These studies demonstrate that the mammalian PNP is a biomechanically coupled structure (Fig. 7*C*) in which neural fold medial apposition is aided by constriction of the caudoventral NMP zone, which narrows the rostral zippering point angle across which cellular protrusions must reach and facilitates the progression of closure.

The closing PNP progressively shortens and narrows with advancing somite stage, and the zippering point is critically involved in PNP shortening; genetic disruption of surface ectoderm cellular protrusions normally formed at this point prevents completion of closure (20, 43). Here we show that the zippering point also serves a biomechanical function, with its physical ablation resulting in rapid lateral displacement of the neural folds and consequent PNP widening. Biomechanically active components involved in NT formation have been studied primarily in *Xenopus*, in which apical constriction has been implicated in bending of the bilayered neuroepithelium (14, 19, 44). Actomyosin contraction is an evolutionarily conserved force-generating mechanism, with resulting forces transmitted between biomechanically coupled cells primarily through cadherin/catenin adherens junctions (45, 46).

The marked apical enrichment of actomyosin that we observe in NMP zone cells is consistent with apical constriction of these cells aiding medial apposition of the neural folds toward the midline as a biomechanically coupled unit. We have demonstrated that biomechanical coupling of the mammalian PNP involves a long-range F-actin cable that extends from the zippering point rostrally, runs along the neural folds as a continuous structure across cell–cell junctions where it colocalizes with E-cadherin, and joins the apically-enriched actomyosin network of the NMP zone cells caudally. In the present study, ablation of functional landmarks which involve the F-actin cable resulted in PNP widening. Similar tension-bearing F-actin cables or rings form during zebrafish epiboly (47), chick amniogenesis (48) mouse eyelid closure (49, 50), and *Drosophila* dorsal closure (51, 52), suggesting an evolutionarily conserved mechanism of transmitting forces across many cell diameters.

The findings of this study suggest that the cellular programs underlying PNP narrowing, which is enhanced by apical constriction in the NMP zone, are likely distinct from those regulating surface ectoderm-mediated cellular protrusions required for PNP shortening (20, 43). In support of this idea, we recently found that preventing actin turnover abrogates the progression of mouse PNP closure, whereas treatment with actomyosin inhibitors at concentrations compatible with continued development in culture does not significantly delay zippering (17, 53). Indeed, because different cell types (neural vs. surface ectoderm) are involved in PNP narrowing and shortening, it seems reasonable that these cell types may be susceptible to different genetic or environmental impediments, leading to spina bifida through distinct mechanisms.

Clustered cases of distal lumbosacral spina bifida observed in human patients (36) have led to the suggestion that a final

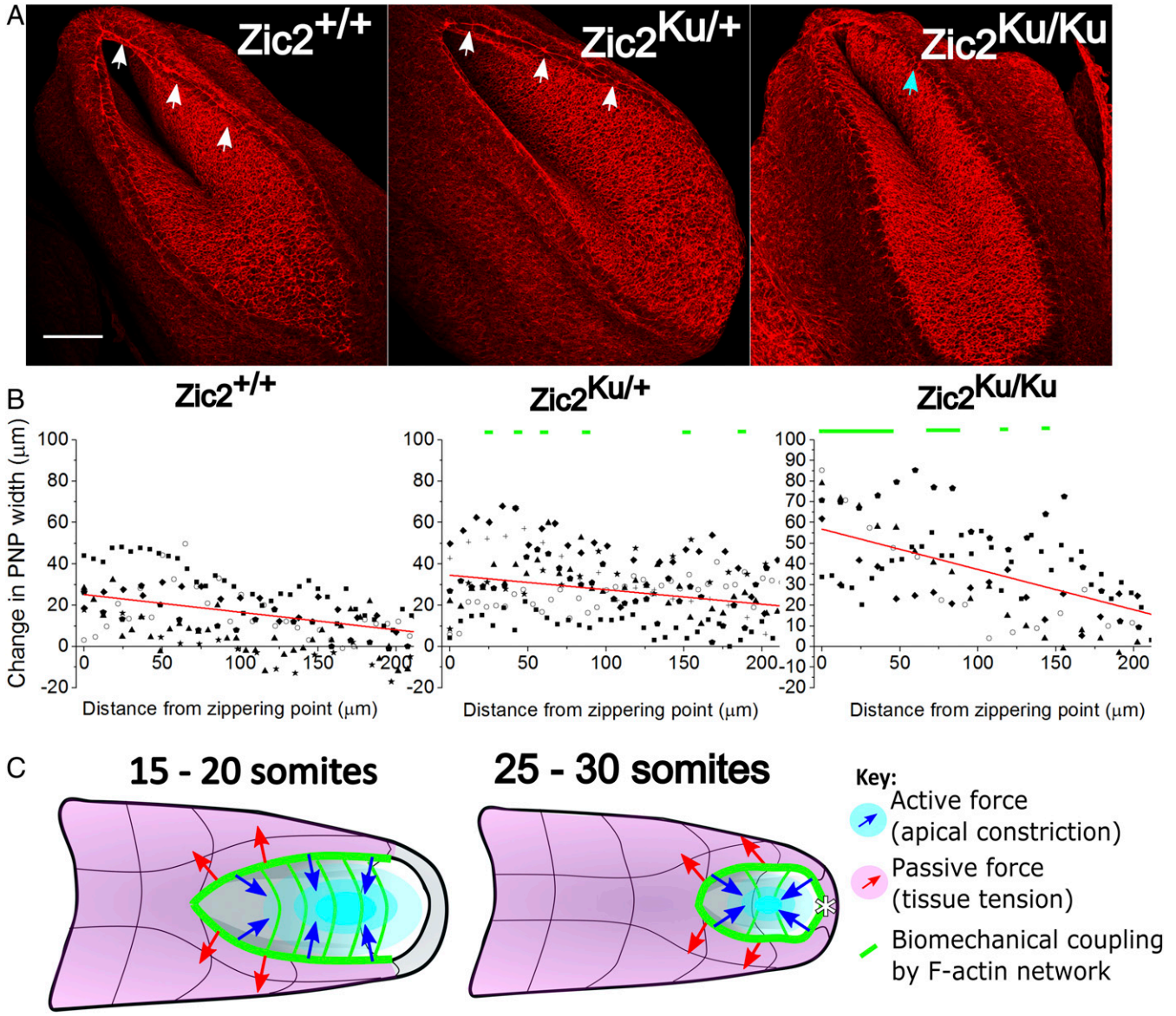

Fig. 7. Zippering point ablation results in greater PNP widening in *Zic2*$^{Ku/Ku}$ mutants than in wild-type littermates. (*A*) Whole mount phalloidin-labeled images of 13 somite wild-type, heterozygous, and homozygous *Zic2*^{Ku} embryos illustrating the characteristic appearance of the PNPs. At this stage, PNP length is not significantly different among the three genotypes. Arrows indicate the F-actin cable, which is markedly less well defined in the *Zic2*$^{Ku/Ku}$ genotype (cyan arrow). (Scale bar: 100 μm.) (*B*) Quantification of the change in PNP width (final width − initial width) at sequential positions caudal to the zippering point in embryos after zippering point laser ablation. Green lines indicate positions at which the *Zic2*$^{Ku/+}$ ($n = 8$) or *Zic2*$^{Ku/Ku}$ ($n = 5$) embryos showed significantly greater increases in width compared with their *Zic2*$^{+/+}$ littermates ($n = 5$). Individual distances from the zippering point were compared by Bonferroni post hoc correction following mixed model analysis, accounting for repeated measures from each embryo. Different symbols indicate values from different embryos. (*C*) Schematic summary of the findings of this study. Constriction of the NMP zone (cyan) actively generates mechanical force (blue arrows) acting on the biomechanically coupled PNP. This opposes stresses within the surrounding tissues (red arrows), facilitating midline apposition of the neural folds, narrowing the zippering point angle and allowing zippering to progress. Encircling of the PNP by the F-actin cable (thick green line) and formation of closure 5 (asterisk in right image) permits the caudal PNP canthus to biomechanically facilitate neural fold apposition when completion of closure is imminent.

closure initiation point may be involved in completion of PNP closure. This final closure has been referred to as the "fourth fusion" (35), or closure 5 (36), but its existence has not been experimentally demonstrated in any mammal (54). In the present study, we found that the caudal canthus of the PNP forms a new zippering structure that not only is characterized by cellular protrusions, which typify the main zippering point (20), but also functionally contributes to late PNP narrowing, given that its disruption by laser ablation results in rewidening of the PNP. Thus, this work provides functional evidence for an active closure mechanism at the caudal extremity, closure 5, which arises late in spinal neurulation.

A limitation of the short-term interventions described here is that their consequences for continuation of spinal closure cannot be directly investigated. For this reason, we studied the *Zic2*$^{Ku/Ku}$ mutant, a well-characterized genetic model in which homozygous mutants develop spina bifida but most heterozygous embryos achieve closure (38). A mechanical basis for spina bifida in the *Zic*$^{Ku/Ku}$ mutant has been suggested, because these embryos display neural folds that fail to bend toward the midline at dorsolateral hinge points (6). We observed that the F-actin cable appeared fragmented in *Zic2*$^{Ku/Ku}$ mutants, which is consistent with a previous report that morpholino-mediated knockdown of

Zic transcription factors in zebrafish disrupts the contiguous actomyosin "apical seam" that normally forms along the presumptive hindbrain lumen (55). Failure of spinal closure in the *Zic2*$^{Ku/Ku}$ mutant was found to be associated with altered PNP biomechanics, resulting in greater PNP rewidening after zippering point ablation. The cellular basis of the altered PNP biomechanics in the *Zic2* mutant embryos is currently unknown, although the observation that Zic2 is expressed almost solely in the neuroepithelium during spinal neurulation (6) suggests that a neuroepithelial defect is likely responsible.

In conclusion, spinal NT closure in the mouse embryo is facilitated by apical constriction of cells within the NMP zone to which the neural folds are biomechanically coupled by an extensive actomyosin network (Fig. 6*C*), including an F-actin cable that demarcates the boundary between the PNP and the E-cadherin expressing surface ectoderm. This biomechanical coupling is genetically influenced, at least in part, by activity of Zic2. Therefore, we propose that genetically influenced biomechanical morphogenetic disorders may be an important cause of spina bifida.

Materials and Methods

Animal Procedures. Studies were performed under project license no. 70/7469 under the United Kingdom Animals (Scientific Procedures) Act 1986 and the Medical Research Council's Responsibility in the Use of Animals for Medical Research (1993). Mice were time-mated overnight, and the morning on which a copulation plug was identified was considered E0.5. Heterozygous *Grhl3*^{Cre}, *Nkx1-2*^{CreERT2}, and *β-actin*^{CreERT2} were as described previously (20, 56–58) and were maintained on a C57BL/6 background. ERT2 activity was induced by i.p. injection of 0.2 mg/40 g body weight of tamoxifen (Sigma-Aldrich) at E8.5. To generate mosaic fluorescent cell patterns in the PNP, heterozygous Cre-expressing mice were crossed with homozygous ROSA26-EYFP mice (20) or mTmG mice (59). Cre-negative mice were used for studies requiring nontransgenic mice. *Zic2*^{Ku} mutants and their genotyping were as described previously (6).

Embryo Dissection and Pharmacologic Treatment. Embryos were harvested at around E9.5 as described previously (60). For whole mounts, embryos were dissected and rinsed in PBS before fixation in 4% paraformaldehyde, pH 7.4. For LatB (Sigma-Aldrich) treatments, embryos were fully dissected from the amnion and prewarmed for 30 min in DMEM containing 10% FBS before addition of LatB or DMSO vehicle, and then fixed after 15 min of treatment. Fixed embryos were stained with CellMask Green (Thermo Fisher Scientific), and their PNPs were imaged on a fluorescence stereo microscope (Leica MZ FIII, with a DC500 camera). PNP midpoint widths were analyzed in ImageJ (61).

Laser Ablation and Live Embryo Imaging. For ablations, embryos were dissected from the amnion, positioned in wells cut out of 4% agarose gel in DMEM, submerged in dissection medium, and maintained at 37 °C throughout imaging. Microsurgical needles from 11–0 Mersilene (TG140-6; Ethicon) and 10–0 Prolene (BV75-3; Ethicon) were used to hold the embryos in place with the PNP pointing upward while minimizing contact with the heart, which continued to beat steadily throughout each experiment. Images were captured on a Zeiss Examiner LSM880 confocal microscope using a 20×/NA1.0 Plan Apochromat dipping objective. If intended for strain mapping, embryos were imaged with *x/y* pixel sizes of 0.59 μm and a Z-step of 1.0 μm, taking ∼7–10 min to image a PNP (speed setting, 8; bidirectional imaging, 1,024 × 1,024 pixels). To measure PNP widths without strain mapping, embryos were typically imaged with *x/y* pixel sizes of 1.2 μm and Z-step of 2.4 μm, taking ∼2–4 min to image a single PNP using reflection mode (MBS T80/R20 beam filter). Before and after ablation, images for each embryo were captured using the same settings. Resulting Z-stacks were reoriented and resliced in Imaris version 8, minimizing changes due to drift or embryo movement between Z stacks.

Laser ablations were performed on a Zeiss Examiner LSM880 confocal microscope using a 20×/NA1.0 Plan Apochromat dipping objective and a SpectraPhysics Mai Tai eHP DeepSee multiphoton laser (800 nm wavelength, 100% laser power, 65.94 μs pixel dwell time, 0.83 μs pixel size, one iteration). A 300- to 500-μm line of closed NT roof was ablated along the embryonic midline by ablating each section within the focal plane. Ablation instantly vaporized a narrow region of tissue, as described previously in mouse embryos (62).

For live imaging, embryos were dissected in an intact yolk sac as for long-term embryo culture (60) and positioned in agarose wells as described above. A small window was made in a minimally vascular part of the yolk sac, and the amnion over the PNP was removed to allow direct visualization of the PNP. All embryos were kept at 37 °C in neat rat serum exposed to 5% CO_2/5% N_2 in air in a custom-made chamber (Solent Scientific) humidified with damp cotton wool. PNPs were imaged with *x/y* pixel sizes of 0.59 μm and a Z-step of 2.5 μm, taking ∼10 min to image each PNP. All embryos had a normal heartbeat and yolk sac circulation throughout imaging.

Whole Mount Staining. All images are representative of observations in at least three independent embryos. Scanning electron microscopy was performed as described previously (20). Mouse anti-E-cadherin antibody (BD Transduction Laboratories), rabbit anti-pMLCII (Ser19; Cell Signaling Technology), mouse anti-total β-catenin (Santa Cruz Biotechnology), and Alexa Fluor 568-conjugated phalloidin (Life Technologies) were used. Paraformaldehyde-fixed embryos were permeabilized in PBS with 0.1% Triton X-100 (PBT) for 1 h at room temperature, blocked overnight in a 5% BSA/PBT at 4 °C, and then incubated overnight in a 1:150 dilution of primary antibody in blocking solution at 4 °C. After three 1-h washings at room temperature in blocking solution, embryos were incubated for 2 h at room temperature in a 1:300 dilution of Alexa Fluor-conjugated secondary antibodies (Thermo Fisher Scientific), a 1:200 dilution of phalloidin, and 0.5 μg/mL DAPI in blocking solution. Excess secondary antibody was removed by washing for 1 h in blocking solution and two more 1-h washings in PBT at room temperature. Stained embryos were imaged on a Zeiss Examiner LSM880 confocal microscope. The high-resolution images shown in *SI Appendix*, section 1, Fig. S5*B* were obtained with Airyscan in SR mode, 2× zoom, with optimal pixel size and Z-step (*x/y* pixel size, 0.065 μm; Z-step, 0.36 μm). Alexa Fluor 568 fluorescence from 570 to 620 nm was collected through a LP570 secondary beam splitter and the Airyscan filter wheel with a BP495-620. Images were processed with Zen2.3 software using auto Airyscan processing.

Strain Mapping. Application of DIC was done according to the software authors' instructions, as described in more detail in *SI Appendix*, section 2. Application of TDSM is also described in further detail in *SI Appendix*, sections 2 and 3, and the software code is provided in Datasets S1–S5. In brief, live imaged PNPs before and after zippering point ablation were digitally resliced in Imaris version 8 to ensure equivalent positioning, and the ImageJ 3D object counter was used to map cell centroids. The *x/y/z* centroids of cells identified in both "before" and "after" images were exported to TDSM, which describes Delaunay triangulations between the same centroids before and after ablation with the zippering point normalized to the graph origin. The percentage change in 2D area of each Delaunay triangle in the 3D meshwork was then calculated. Heat maps were generated in OriginPro 2016 (Origin Labs) as the aggregate of data from three independent embryos in each group.

Strain maps were generated using three Cre drivers. Grhl3Cre is mosaic in the mesoderm and neuroepithelium but ubiquitous in the surface ectoderm; strain maps generated using this driver include only mesodermal and neuroepithelial cells. β-actin Cre^{ERT2} was induced at a low recombination rate in all cell types. The Nkx1-2 Cre^{ERT2} lineage traces both mesodermal and neuroepithelial cell types, but only cells within the caudoventral PNP with a neuroepithelial morphology were analyzed. Imaging depth was approximately 100 μm from the surface, such that strain maps represent cells up to 100 μm deep into the tissue.

Statistical Analysis. Comparisons between two groups were performed with Student's unpaired *t* test, accounting for homogeneity of variance, using Microsoft Excel or in SPSS version 22 (IBM). Comparison of multiple groups was done by one-way ANOVA with Bonferroni's post hoc correction in SPSS version 22. Linear regression was done using OriginPro 2016 (Origin Labs). Multivariate analysis was performed using linear mixed models in SPSS version 22 accounting for the fixed effects of genotype, time, or distance from the zippering point in repeated measures from each embryo (random variable) as appropriate for the analysis, with a Bonferroni post hoc correction where applicable. Analysis of PNP widening in the *Kumba* embryos was performed blinded before genotyping. Graphs were created in OriginPro 2016 and are represented as raw data points or boxplots when single groups are shown per measurement level, or as mean ± SEM when several groups are shown per measurement level. $P < 0.05$ was considered statistically significant.

ACKNOWLEDGMENTS. We thank Mark Turmaine for assistance with SEM imaging; Oleksandr Nychyk, Amy Hughes, and José Manuel Caro Vega for technical assistance; and Alastair Poole for critical discussions. This project was funded primarily by a Wellcome Trust Postdoctoral Training Fellowship for Clinicians (107474/Z/15/Z, to G.L.G.), and also by grants from the Wellcome

Trust (087525, to A.J.C. and N.D.E.G.) the Medical Research Council (J003794, to N.D.E.G. and A.J.C.), and the Bo Hjelt Spina Bifida Foundation (to A.J.C.). N.D.E.G. is supported by Great Ormond Street Hospital Children's Charity. The authors alone are responsible for the content of this paper, which does not necessarily represent the decisions, policy, or views of the World Health Organization or its member states.

1. Morris JK, et al. (2016) Prevention of neural tube defects in the UK: A missed opportunity. *Arch Dis Child* 101:604–607.
2. Van Straaten HW, Janssen HC, Peeters MC, Copp AJ, Hekking JW (1996) Neural tube closure in the chick embryo is multiphasic. *Dev Dyn* 207:309–318.
3. van Straaten HW, Peeters MC, Hekking JW, van der Lende T (2000) Neurulation in the pig embryo. *Anat Embryol (Berl)* 202:75–84.
4. Ray HJ, Niswander LA (2016) Dynamic behaviors of the non-neural ectoderm during mammalian cranial neural tube closure. *Dev Biol* 416:279–285.
5. Henrique D, Abranches E, Verrier L, Storey KG (2015) Neuromesodermal progenitors and the making of the spinal cord. *Development* 142:2864–2875.
6. Ybot-Gonzalez P, et al. (2007) Neural plate morphogenesis during mouse neurulation is regulated by antagonism of Bmp signalling. *Development* 134:3203–3211.
7. His W (1894) Über mechanische Grundvorgänge thierischer Formbildung [On the mechanical basis of animal morphogenesis]. Arch Anat Physiol u wiss Med: Anat Abth, 1–80. German.
8. Miller ME, Graham JM, Jr, Higginbottom MC, Smith DW (1981) Compression-related defects from early amnion rupture: Evidence for mechanical teratogenesis. *J Pediatr* 98:292–297.
9. Brook FA, Shum AS, Van Straaten HW, Copp AJ (1991) Curvature of the caudal region is responsible for failure of neural tube closure in the curly tail (ct) mouse embryo. *Development* 113:671–678.
10. van Straaten HW, Hekking JW, Consten C, Copp AJ (1993) Intrinsic and extrinsic factors in the mechanism of neurulation: Effect of curvature of the body axis on closure of the posterior neuropore. *Development* 117:1163–1172.
11. Hashimoto H, Robin FB, Sherrard KM, Munro EM (2015) Sequential contraction and exchange of apical junctions drives zippering and neural tube closure in a simple chordate. *Dev Cell* 32:241–255.
12. Benko R, Brodland GW (2007) Measurement of in vivo stress resultants in neurulation-stage amphibian embryos. *Ann Biomed Eng* 35:672–681.
13. Brodland GW, Chen X, Lee P, Marsden M (2010) From genes to neural tube defects (NTDs): Insights from multiscale computational modeling. *HFSP J* 4:142–152.
14. Inoue Y, et al. (2016) Mechanical roles of apical constriction, cell elongation, and cell migration during neural tube formation in *Xenopus*. *Biomech Model Mechanobiol* 15:1733–1746.
15. Sokol SY (2016) Mechanotransduction during vertebrate neurulation. *Curr Top Dev Biol* 117:359–376.
16. Vijayraghavan DS, Davidson LA (2016) Mechanics of neurulation: From classical to current perspectives on the physical mechanics that shape, fold, and form the neural tube. *Birth Defects Res A Clin Mol Teratol* 109:153–168.
17. Escuin S, et al. (2015) Rho-kinase-dependent actin turnover and actomyosin disassembly are necessary for mouse spinal neural tube closure. *J Cell Sci* 128:2468–2481.
18. Grego-Bessa J, Hildebrand J, Anderson KV (2015) Morphogenesis of the mouse neural plate depends on distinct roles of cofilin 1 in apical and basal epithelial domains. *Development* 142:1305–1314.
19. Ossipova O, et al. (2014) Role of Rab11 in planar cell polarity and apical constriction during vertebrate neural tube closure. *Nat Commun* 5:3734.
20. Rolo A, et al. (2016) Regulation of cell protrusions by small GTPases during fusion of the neural folds. *eLife* 5:e13273.
21. Lewis WH (1947) Mechanics of invagination. *Anat Rec* 97:139–156.
22. Jacobson AG, Gordon R (1976) Changes in the shape of the developing vertebrate nervous system analyzed experimentally, mathematically and by computer simulation. *J Exp Zool* 197:191–246.
23. Morita H, et al. (2012) Cell movements of the deep layer of non-neural ectoderm underlie complete neural tube closure in *Xenopus*. *Development* 139:1417–1426.
24. Beloussov LV, Dorfman JG, Cherdantzev VG (1975) Mechanical stresses and morphological patterns in amphibian embryos. *J Embryol Exp Morphol* 34:559–574.
25. Carriero A, Abela L, Pitsillides AA, Shefelbine SJ (2014) Ex vivo determination of bone tissue strains for an in vivo mouse tibial loading model. *J Biomech* 47:2490–2497.
26. Begonia MT, et al. (2015) Non-contact strain measurement in the mouse forearm loading model using digital image correlation (DIC). *Bone* 81:593–601.
27. Khodabakhshi G, et al. (2013) Measuring three-dimensional strain distribution in tendon. *J Microsc* 249:195–205.
28. van Straaten HW, Hekking JW, Copp AJ, Bernfield M (1992) Deceleration and acceleration in the rate of posterior neuropore closure during neurulation in the curly tail (ct) mouse embryo. *Anat Embryol (Berl)* 185:169–174.
29. Wang Z, Kieu H, Nguyen H, Le M (2015) Digital image correlation in experimental mechanics and image registration in computer vision: Similarities, differences and complements. *Opt Lasers Eng* 65:18–27.
30. Jones EMC, Silberstein MN, White SR, Sottos NR (2014) In situ measurements of strains in composite battery electrodes during electrochemical cycling. *Exp Mech* 54:971–985.
31. Li F, Chan CU, Ohl CD (2013) Yield strength of human erythrocyte membranes to impulsive stretching. *Biophys J* 105:872–879.
32. Yuan F, Yang C, Zhong P (2015) Cell membrane deformation and bioeffects produced by tandem bubble-induced jetting flow. *Proc Natl Acad Sci USA* 112:E7039–E7047.
33. Rolo A, Skoglund P, Keller R (2009) Morphogenetic movements driving neural tube closure in *Xenopus* require myosin IIB. *Dev Biol* 327:327–338.
34. Sadler TW, Greenberg D, Coughlin P, Lessard JL (1982) Actin distribution patterns in the mouse neural tube during neurulation. *Science* 215:172–174.
35. Sakai Y (1989) Neurulation in the mouse: Manner and timing of neural tube closure. *Anat Rec* 223:194–203.
36. Van Allen MI, et al. (1993) Evidence for multi-site closure of the neural tube in humans. *Am J Med Genet* 47:723–743.
37. Seller MJ (1995) Further evidence for an intermittent pattern of neural tube closure in humans. *J Med Genet* 32:205–207.
38. Elms P, Siggers P, Napper D, Greenfield A, Arkell R (2003) Zic2 is required for neural crest formation and hindbrain patterning during mouse development. *Dev Biol* 264: 391–406.
39. Shivakumar PC, Lenne PF (2016) Laser ablation to probe the epithelial mechanics in *Drosophila*. *Methods Mol Biol* 1478:241–251.
40. Vogel A, Venugopalan V (2003) Mechanisms of pulsed laser ablation of biological tissues. *Chem Rev* 103:577–644.
41. Keller R, Davidson LA, Shook DR (2003) How we are shaped: The biomechanics of gastrulation. *Differentiation* 71:171–205.
42. Hardin J (1988) The role of secondary mesenchyme cells during sea urchin gastrulation studied by laser ablation. *Development* 103:317–324.
43. Rolo A, Escuin S, Greene ND, Copp AJ (2016) Rho GTPases in mammalian spinal neural tube closure. *Small GTPases*, doi.org/10.1080/21541248.2016.1235388.
44. Christodoulou N, Skourides PA (2015) Cell-autonomous Ca(2+) flashes elicit pulsed contractions of an apical actin network to drive apical constriction during neural tube closure. *Cell Reports* 13:2189–2202.
45. Heisenberg CP, Bellaïche Y (2013) Forces in tissue morphogenesis and patterning. *Cell* 153:948–962.
46. Vasquez CG, Martin AC (2016) Force transmission in epithelial tissues. *Dev Dyn* 245: 361–371.
47. Chai J, et al. (2015) A force balance can explain local and global cell movements during early zebrafish development. *Biophys J* 109:407–414.
48. Tipping N, Wilson D (2011) Chick amniogenesis is mediated by an actin cable. *Anat Rec (Hoboken)* 294:1143–1149.
49. Hislop NR, et al. (2008) Grhl3 and Lmo4 play coordinate roles in epidermal migration. *Dev Biol* 321:263–272.
50. Heller E, Kumar KV, Grill SW, Fuchs E (2014) Forces generated by cell intercalation tow epidermal sheets in mammalian tissue morphogenesis. *Dev Cell* 28:617–632.
51. Pasakarnis L, Frei E, Caussinus E, Affolter M, Brunner D (2016) Amnioserosa cell constriction but not epidermal actin cable tension autonomously drives dorsal closure. *Nat Cell Biol* 18:1161–1172.
52. Ducuing A, Vincent S (2016) The actin cable is dispensable in directing dorsal closure dynamics but neutralizes mechanical stress to prevent scarring in the *Drosophila* embryo. *Nat Cell Biol* 18:1149–1160.
53. Ybot-Gonzalez P, Copp AJ (1999) Bending of the neural plate during mouse spinal neurulation is independent of actin microfilaments. *Dev Dyn* 215:273–283.
54. Copp AJ, Stanier P, Greene ND (2013) Neural tube defects: Recent advances, unsolved questions, and controversies. *Lancet Neurol* 12:799–810.
55. Nyholm MK, Abdelilah-Seyfried S, Grinblat Y (2009) A novel genetic mechanism regulates dorsolateral hinge-point formation during zebrafish cranial neurulation. *J Cell Sci* 122:2137–2148.
56. Lewandoski M, Martin GR (1997) Cre-mediated chromosome loss in mice. *Nat Genet* 17:223–225.
57. Camerer E, et al. (2010) Local protease signaling contributes to neural tube closure in the mouse embryo. *Dev Cell* 18:25–38.
58. Rodrigo Albors A, Halley PA, Storey KG (2016) Fate mapping caudal lateral epiblast reveals continuous contribution to neural and mesodermal lineages and the origin of secondary neural tube. *bioRxiv*, doi: https://doi.org/10.1101/045872.
59. Muzumdar MD, Tasic B, Miyamichi K, Li L, Luo L (2007) A global double-fluorescent Cre reporter mouse. *Genesis* 45:593–605.
60. Pryor SE, Massa V, Savery D, Greene ND, Copp AJ (2012) Convergent extension analysis in mouse whole embryo culture. *Methods Mol Biol* 839:133–146.
61. Schindelin J, et al. (2012) Fiji: An open-source platform for biological-image analysis. *Nat Methods* 9:676–682.
62. Angelo JR, Tremblay KD (2013) Laser-mediated cell ablation during post-implantation mouse development. *Dev Dyn* 242:1202–1209.